Lift Enhancement through Flexibility of Plunging Wings at Low Reynolds Numbers

D.J. Cleaver, D.E. Calderon, Z. Wang and I. Gursul

Department of Mechanical Engineering, University of Bath, Bath, BA2 7AY, UK

Abstract

In this paper the combined effect of two mechanisms for lift enhancement at low Reynolds numbers are considered, wing oscillations and wing flexibility. The force, deformation and flow fields of rigid and flexible low aspect ratio (AR = 3) and high aspect ratio (AR = 6) wings oscillating at a fixed *post-stall* angle of attack of 15° and amplitude of 15% of chord are measured. The force measurements show that flexibility can increase the time-averaged lift coefficient significantly. For low aspect ratio wings the maximum lift coefficient across all Strouhal numbers was C_l = 1.38 for the rigid wing as opposed to C_l = 2.77 for the flexible wing. Very similar trends were observed for the high aspect ratio wings. This increase is associated with significant deformation of the wing. The root is sinusoidally plunged with small amplitude but this motion is amplified along the span resulting in a larger tip motion but with a phase lag. The amount it is amplified strongly depends on Strouhal number. A Strouhal number of Sr_c = 1.5 was selected for detailed flow field measurements due to it being central to the high-lift region of the flexible wings, producing approximately double the lift of the rigid wing. For this Strouhal number the rigid wings exhibit a Leading Edge Vortex (LEV) ring. This is where the clockwise upper-surface LEV pairs with the counter-clockwise lower-surface LEV to form a vortex ring that self-advects upstream and away from the wing's upper surface. Conversely the deformation of the flexible wings inhibits the formation of the LEV ring. Instead a strong upper-surface LEV forms during the downward motion and convects close to the airfoil upper surface thus explaining the significantly higher lift. These measurements demonstrate the significant gains that can be achieved through the combination of unsteady aerodynamics with flexible structures.

1. Introduction

For decades researchers and scientists have been fascinated by natural flight both in its own right, and also as inspiration for Micro Air Vehicles (MAVs). The truly exceptional performance of birds and insects, in terms of speed and agility, often exceeds man made aircraft on a like-for-like basis (Shyy *et al*., 1999). During the latter part of the 20th century it has become clear that this exceptional performance is far greater than that achievable under steady or quasi-steady conditions. It is therefore reasonable to suppose that natural flyers employ unsteady mechanisms to overcome deteriorating aerodynamic performance at low Reynolds numbers. Of the unsteady aerodynamic phenomenon the Leading Edge Vortex (LEV) is generally accepted (Ho *et al*., 2003; Sane, 2003) as being responsible for creating the majority of the large time-averaged lift force, making it crucial for low Reynolds number flapping flight.

We have previously shown (Cleaver *et al*., 2011) that, in the post-stall regime, similar LEVs and high time-averaged lift coefficients can be created for an airfoil undergoing a small-amplitude high-frequency motion that is more suited to man made actuators. The maximum time-averaged lift coefficient observed was 305% larger than that achieved by the stationary wing and was also accompanied by thrust generation. This improvement is due to convected LEVs. The behavior of these convected LEVs is strongly dependent on airfoil geometry (Cleaver *et al*., 2013a). For a flat plate and NACA 0012 airfoil at low Strouhal numbers ($Sr_c = fc/U_\infty < 1$) the behavior is qualitatively similar, lift increase that is amplified at the natural shedding frequency and its harmonics / subharmonics; but at high Strouhal numbers ($Sr_c > 1$), for the same experimental conditions, a thin flat plate geometry experiences deteriorating lift and high drag. This is due to the formation of a LEV dipole. This is where the upper surface LEV pairs with the lower surface LEV to form a dipole that self-advects upstream away from the airfoil surface. This LEV dipole rapidly loses its coherency but results in a highly separated time-averaged flow and thus low lift and high drag.

Similar behavior is also observed for flat plate finite wings (Calderon *et al*., 2013a) including a range of planforms (Calderon *et al*., 2013b). At lower Strouhal numbers lift increases with peaks around the natural shedding frequency but at higher Strouhal numbers lift performance deteriorates. This is associated with the formation of a LEV ring structure that directs flow upstream and dissipates the LEV. This behavior is most apparent in Figure 16 of Calderon *et al*. (2013a). This shows the rapid dissipation of

the upper-surface LEV in a manner that is qualitatively identical to the flat plate airfoil. The effect on the three-dimensional flow field is shown in Figure 17 (Calderon *et al*., 2013a). This shows a LEV that is strong and coherent near the tip but loses coherency towards the root resulting in breakdown of the vortex. In addition for these finite wings very complex tip vortex interactions are observed that are attributed (Calderon *et al*., 2013b) with increasing lift. This is similar to natural flight where the tip vortex has been attributed (Shyy *et al*., 2009) with increasing lift by creating a low-pressure region and delaying / preventing LEV shedding.

A further aspect of natural flight is the aeroelastic interaction of the lightweight structure with the large inertial forces which inevitably leads to deformation (Mountcastle & Daniel, 2009; Biewener & Dial, 1995). There is a small but growing body of evidence that this passive deformation can improve lift and thrust generation although the exact detail and mechanisms remain unresolved (Mountcastle & Daniel, 2009). For periodically plunging wings, several studies for chordwise (Heathcote & Gursul, 2007; Shyy *et al*., 2010; Cleaver *et al*., 2014) and spanwise (Shyy *et al*., 2010, Heathcote *et al*., 2008; Chimakurthi *et al*. 2009) flexibility have shown that optimal flexibility, and therefore deformation, can improve thrust performance in terms of both time-averaged thrust coefficient and propulsive efficiency. For the chordwise flexible cases the thrust was improved through stronger trailing-edge vortices spaced further apart leading to a stronger time-averaged jet. For spanwise flexible wings, operating at $Sr_A=fA/U_\infty$ greater than 0.2, appropriate flexibility was found to simultaneously increase thrust coefficient slightly and reduce power coefficient slightly resulting in increased efficiency. Chimakurthi *et al*. (2009) postulated that the increased thrust was a result of higher local instantaneous effective angles of attack, promoting larger streamline curvatures and thus greater leading-edge suction.

In terms of the effect on lift generation, it has previously been demonstrated that flexibility can be beneficial for lift generation on delta wings (Taylor *et al*., 2007). In this case the flexibility led to self-excited wing vibrations through aeroelastic interactions. Similarly, self-excited membrane vibrations can cause a delay in stall for membrane wings as demonstrated numerically (Gordnier, 2009) and experimentally (Rojratsirikul *et al*., 2011). However, to the author's knowledge no previous studies have experimentally considered the effect of flexibility on lift coefficient for *flexible plunging wings* in the post-stall regime. This is potentially a viable method of increasing

lift coefficient at low Reynolds numbers in an efficient manner. A computational study (Barnes et al., 2013) for the same experimental parameters as in this article has shown that flexibility of a wing plunging at the root with small amplitude can increase time-averaged lift significantly demonstrating its potential. This lift increase through flexibility was attributed to two factors: a) a stronger tip vortex and b) inhibition of the LEV ring described above.

The main objective of this paper is to study the effect of flexibility on lift performance of plunging wings in the post-stall regime. Force, deformation and three-dimensional defocused digital particle image velocimetry (here termed volumetric velocimetry) measurements are presented for rigid and flexible flat plate wings of low and high aspect ratio (AR = 3 and 6) oscillating with small-amplitude (a/c = 0.15) and range of Strouhal number ($Sr_c \leq 2.025$). These measurements fully characterize the relation between time-averaged force, phase-averaged deformation and phase-averaged flow fields.

2. Experimental Apparatus and Procedures

Force, Digital Image Correlation (DIC) and volumetric velocimetry measurements were conducted for plunging rigid and flexible wings mounted vertically in a closed-loop water tunnel, see Fig. 1 (a). For a review of parameters studied, see Table 1; uncertainties are calculated based on the methods of Moffat (1988) taking into account both bias and precision errors. Note that Strouhal number is directly related to the reduced frequency through: $Sr_c = k/\pi$.

Table 1 Experimental Parameters

Parameter	Range Considered	Uncertainty
Re	10,000	+/- 200
α	15°	+/- 0.5°
a/c	0.15	+/- 0.003
Sr_c	0 to 2.025	+/- 2.3%

2.1 Experimental Setup

The experiments were conducted in a free-surface closed-loop water tunnel (Eidetics Model 1520) at the University of Bath. The water tunnel is capable of flow speeds in the range U_∞=0 to 0.5 m/s and has a working section of dimensions 381 mm x 508 mm x 1530 mm. The turbulence intensity has previously (Heathcote, 2006) been measured by LDV to be less than 0.5%.

Mounted on top of the tunnel is the experimental rig, see Fig. 1 (a). The oscillations were supplied via a Motavario 0.37 kW three-phase motor, 5:1 wormgear and IMO Jaguar Controller. The position of the root of the airfoil was measured through a rotary encoder attached to the spindle of the worm gear shaft. The rotary encoder was also used to trigger the DIC, volumetric velocimetry system and determine the instantaneous plunge velocity for the calculation of the power coefficient.

In this paper two aspect ratios are considered. For the *low aspect ratio* (full aspect ratio *AR*=3 or semi-aspect ratio *sAR*=1.5) case one rigid and four flexible wings are considered. All low AR wings have right-angled leading and trailing edges, and dimensions of c=0.1 m chord and s=0.15 m span, see Fig 2 (c). The rigid wing (t = 0.015c) is manufactured from mild steel. The flexible wings (t = 0.01c) are manufactured from PTFE, polypropylene, polycarbonate and nylon, see Table 2 for material properties. The bending stiffness coefficient for spanwise deformation is defined as (Gursul et al., 2014):

$$\lambda = \frac{EI}{\frac{1}{2}\rho U_\infty^2 S b^2}$$

where S is the area and b the span of the flexible portion of the wing. Table 2 shows that the rigid wing is orders of magnitude more rigid than the flexible. In Table 2 the natural frequency is measured by applying an impulsive motion to the wing in stationary water and then measuring the frequency of the oscillations in lift. For *sAR* = 1.5 the measured natural frequency does not scale monotonically with λ. This is likely due to variation in material density of the flexible wings, varies from 964 kg/m^3 to 2200 kg/m^3, and uncertainty in the value of Young's Modulus for Nylon and Polypropylene. As shown in Fig. 2c the flexible material was clamped in an interchangeable mild steel holder to guarantee chordwise rigidity along the root. The deformation is therefore predominantly spanwise bending. The maximum twist angle measured is 6˚ which is small compared to a peak effective angle of attack of 82˚ (due to mostly plunging /

bending motion). The rigid wing was silver soldered into a similar holder to guarantee rigidity.

Table 2 Flexible Wing Properties

Material	*t*, mm	Young's Modulus, *E*		Bending Stiffness Coefficient, λ	Measured Natural Frequency, Sr_c
		Gpa	Source		
			sAR = 1.5		
Mild Steel ('Rigid')	1.5	210	Matweb	3273	-
Nylon	1	3.00	Matweb	13.1	1.3
Polycarbonate	1	2.30	Manufacturer	9.9	1.6
Polypropylene	1	1.70	Matweb	7.9	1.8
PTFE ('Flexible')	1	0.80	Measured	3.4	1.5
			sAR = 3		
Mild Steel ('Rigid')	4	210	Matweb	7370	-
Acrylic	3	3.05	Matweb	46.6	2.2
Polyethylene ('Flexible')	3	0.90	Measured	13.0	1.5

For the *high aspect ratio* (full aspect ratio *AR*=6 or semi-aspect ratio *sAR* = 3) case one rigid and two flexible wings are considered. All high AR wings have semi-circular leading and trailing edges, and dimensions of 0.1 m chord and 0.3 m span. The rigid wing is manufactured from mild steel (t = 0.04c). The flexible wings (t = 0.03c) are manufactured from acrylic and polyethylene, see Table 2. For the flexible wings the flexible material was bonded into a mild steel holder to guarantee chordwise rigidity along the root, see Fig. 2 (b). Whereas the rigid wing was directly welded to the supporting bars to guarantee rigidity, see Fig. 2 (a).

The wings are rigidly mounted at the root with a fixed angle of attack of $\alpha = 15^0$, see Fig. 3 (a) and driven in a sinusoidal motion, see Fig. 3 (b). The phase of the motion is defined by the normalised time t/T where t/T = 0 is the top of the motion, t/T = 3/12 is the point of maximum downwards velocity, t/T = 6/12 is the bottom of the motion and t/T = 9/12 is the point of maximum upwards velocity.

2.2 Force Measurements

The forces in the cross-stream and streamwise directions were measured through a two-component binocular strain gauge force balance (Frampton *et al.,* 2002). This design has been used in several studies with good accuracy (Cleaver *et al*., 2011 and 2013a; Calderon *et al*., 2013a and b). Two force balances of differing rigidities

were used so as to achieve the desired accuracy whilst minimizing flexibility. The signal from the strain gauges was amplified by a Wheatstone bridge circuit and sampled at either 1 kHz for 20,000 samples (stationary cases), or 360 per cycle (dynamic cases). The forces were then calculated from the average voltage through linear calibration curves. The measured forces included both time-dependent aerodynamic forces as well as inertia forces, however the inertia forces do not contribute to the time-averaged force. The calibration curves consisted of twenty three points, and were performed daily before and after testing. Each data set consists of an average of at least four individual runs.

The uncertainty associated with these time-averaged force measurements generally increases with increasing frequency. For a typical high AR case (λ=46.6) the uncertainty increases from ±0.05 at Sr_c = 0, to ±0.30 at Sr_c=1.5 for lift coefficient, ±0.035 to ±0.083 for drag coefficient and from zero, by definition, to ±2.17 for power coefficient.

2.3 Deformation Measurements

The deformation of the flexible wings was measured with a Limess DIC system. This consists of a pair of Photron SA3 cameras capable of image acquisition with a resolution of 1024 x 1024 pixels at 1,000 fps. Normally these cameras are mounted at an angle to each other to give depth information and the same field of view. In the current scenario this was not appropriate because refraction at the water-glass-air interface leads to image warping which will give erroneous results. To minimise this effect the cameras were instead kept parallel and the angle was created by angling the lenses with Scheimpflug mounts, see Fig. 1b. The images were processed in the software VIC-3D. The calibration consisted of at least 70 images of a randomly orientated 12 x 9 grid. The setup and calibration were validated by performing measurements for the stationary rigid wing as it is manually moved a known distance in the range: 0 to 30 mm. The error was always less than 0.15%c. The majority of results shown herein are instantaneous measurements for Strouhal numbers of Sr_c = 0.075 to 2.025 with a Sr_c = 0.075 interval. These were acquired at a rate of twenty four images per cycle for a minimum of ten cycles. The midchord position, deformation, and twist angle along the span are then derived in MATLAB by taking small 1 mm wide chordwise slices at regular spanwise locations. For each spanwise location a sine curve

is then fitted to the midchord position as a function of time to give amplitude and phase information. Due to the finite subgrid size (size of pixel area for cross-correlation) used in DIC processing it was not possible to perform measurements at $z/s = 0$ or 1. The wings shown in the volumetric velocimetry figures were built from phase-averaged deformation measurements.

2.4 Volumetric Velocimetry measurements

The volumetric flow measurements were acquired using a three-component velocimetry (TSI V3V™) system based on the techniques developed by Pereira & Gharib (2002) for Defocusing Digital Particle Image Velocimetry (DDPIV). The flow was seeded with 50 μm hollow glass particles. The volume of interest was illuminated using a dual Nd:YAG 200 mJ pulsed laser, equipped with two cylindrical lenses offset by 90 degrees from each other to generate a laser cone, see Fig. 4. The laser cones were fired 700 μs apart. The images were acquired using three 4MP 12 bit CCD cameras placed to form an equilateral triangle whose common focal plane defines the most distant plane within the volume of interest. DDPIV uses multiple off-axis apertures to generate multiple defocused particle images where the particle's separation distance and location give its position in three-dimensional space. If the three images of a single particle were superimposed, the particle would appear as a triangle with its centre equating to its x-y coordinates and the size of the triangle equating to its z coordinate. The cameras were calibrated by translating a rectangular plate of regularly spaced grid dots across the volume of interest with image triplets acquired at 5 mm intervals to generate a camera signature graph.

There are four stages from image to gridded velocity data. (i) The particles are identified in each of the six captured images (three images at two separate times), using a 2D particle identification algorithm. (ii) Using the triangles generated during the calibration stage the particles are grouped with their counterparts in the other images to form triplets. The size and location of these triplets gives two sets of three-dimensional particle coordinates equating to the two times. (iii) The particles are 'tracked' through a 3D particle tracking algorithm using the relaxation method first proposed by Baek & Lee (1996). This essentially uses an iterative process to update the probability of two particles matching between two frames, at each time, using neighbour particle displacement similarity criteria as well as flow estimates, and then choosing the particle

match with greatest probability. This is outlined in more detail by Pereira *et al*. (2006). A median filter was applied to remove any outliers. (iv) The randomly spaced vectors from 200 separate phase-locked measurements are interpolated onto a uniformly spaced grid of voxel size 8 mm with a 55% overlap to give phase-averaged uniformly spaced velocity vectors. The grid interpolation produced 25,000 to 37,000 grid vectors within a measurement volume of 140 × 140 × 100 mm.

To capture the entire span, it was necessary to perform measurements separately for multiple volumes from z/s = 0 to 1.33. For the low aspect ratio wings three volumes were performed with the camera below as shown in Fig. 4a. During the upward motion the deformation of the wing obscured the flow in the direct vicinity of the upper surface. Two further volumes were therefore performed with the camera above the upper surface, see Fig. 4b. Due to its larger size the high aspect ratio wing required five volumes with the cameras below and three with the cameras at the side. These multiple volumes are then combined in MATLAB through interpolation onto a common grid. At the same time the desired flow properties such as vorticity magnitude are also calculated. These flow properties were then imported into Tecplot 360™ for plotting, along with a model of the deforming wing built from the deformation measurements.

3. Results and Discussion

This section describes the force, deformation and then flow field measurements for both low and high aspect ratio wings. To be concise it focusses on the low aspect ratio case because, as will be shown, qualitatively similar behavior is observed for both aspect ratios.

3.1 Force measurements

Shown in Fig. 5 are time-averaged lift ($C_L = \overline{F_y}/0.5\rho csU_\infty^2$), drag ($C_D = \overline{F_x}/0.5\rho csU_\infty^2$), and power coefficient ($C_P = \overline{F_y U_{pl}}/0.5\rho csU_\infty^3$) for the rigid and flexible wings oscillating with an amplitude of a/c = 0.15 and α = 15°. The left column is for low aspect ratio; the right column for high aspect ratio. For sAR = 3 and λ = 46.6 typical uncertainty error bars are shown. Also shown in the right column are force measurements for an 'infinite' wing. This wing is identical to the high AR λ=7370 wing

except with a lower end plate added at the tip. The λ=7370 wing is orders of magnitude more rigid than the flexible cases and subject to negligible deformation, it is therefore termed 'rigid'. Due to the negligible deformation and end plates the infinite wing can therefore be considered as a 2D geometry (airfoil). The results for this airfoil have previously been presented (Cleaver *et al*., 2011). The salient features are a general increase in lift coefficient at small plunge velocities to give an almost linear trend with Sr_A due to growing strength of the upper surface leading-edge vortex. Superimposed onto this linear trend are several peaks due to resonance at the natural shedding frequency, its harmonics, and subharmonics. At higher Strouhal numbers there is a gradual reduction in lift coefficient due to the upper surface and lower surface LEVs forming a dipole that convects upwards resulting in increased time-averaged flow separation. This increased time-averaged flow separation is also reflected in the drag coefficient which show that at large Strouhal numbers there is a negligible change in drag coefficient. This is in stark contrast to the very large thrust coefficients (C_d = -2.76) observed for a NACA 0012 airfoil oscillating at identical conditions, demonstrating the importance of airfoil geometry for plunging wings.

The effect of the tip vortex is demonstrated through comparison of the infinite wing with the λ=7370 rigid wing because these are identical except for the tip end plate. Time-averaged lift coefficient for the rigid wing demonstrates the same qualitative trends as the infinite wing except with consistently lower values. Initially this difference is small, but tends to grow with increasing Strouhal number. As a result the maximum lift coefficient is significantly lower: C_l = 1.75 versus 2.59, an increase over the stationary case of 120% for the rigid wing as opposed to 178% for the infinite wing. By contrast the time-averaged drag coefficient is consistently reduced by the three-dimensionality and the comparative improvement grows with increasing Strouhal number. Time-averaged power coefficient shows the same parabolic trend as observed by Heathcote & Gursul (2007) and Young and Lai (2007) except with a slightly shallower gradient for the finite wing.

The effect of flexibility at high aspect ratio is demonstrated by comparison of the λ=7370 wing with the λ=46.6 and 13.0 wings. At low Strouhal numbers (Sr_c < 0.8) there is negligible effect on time-averaged lift coefficient. At higher Strouhal numbers (Sr_c > 0.8) the three curves diverge with increasing flexibility leading to significantly larger lift coefficients. For λ = 13.0 the peak lift coefficient is C_l = 3.07, an increase of

278% over the stationary airfoil. Similarly at low Strouhal numbers there is negligible effect on time-averaged drag coefficient. At $Sr_c \approx 0.8$ the three curves diverge with greater flexibility leading to larger drag coefficient, reflecting the increasing lift coefficient in this range. In terms of power coefficient, at intermediate Strouhal numbers flexibility increases power coefficient. At a flexibility dependent Strouhal number it crosses the rigid power coefficient curve resulting in comparatively lower power at high Strouhal numbers. The value of this crossover is $Sr_c = 1.50$ for λ=13.0 and $Sr_c = 2.025$ for λ=46.6. This behavior is in stark contrast to the established relationships shown for the infinite wing and λ=7370 'Rigid' wing. This difference is because power coefficient is derived from lift fluctuations and instantaneous plunge velocity (U_{pl}). It is therefore subject to both the amplitude and phase of unsteady lift force relative to the plunge velocity. As will be shown later the flexible wings are subject to significant deformation that will both reduce amplitude and introduce a phase lag to the unsteady force. For conciseness the deformation and velocimetry measurements will consider the two extreme high AR cases: λ=7370, termed 'rigid', and λ=13.0, termed 'flexible'. This flexible case was chosen due to the very high lift coefficients at high Strouhal numbers.

The effect of flexibility at low aspect ratio is qualitatively similar. At low Strouhal numbers (Sr_c<0.8) it has minimal effect; at high Strouhal numbers (Sr_c>0.8) the performance diverges with flexibility increasing lift. The lack of a clear optimum flexibility is most likely due to the limited range of flexibilities studied. The maximum recorded lift coefficient is $C_l = 2.77$ for λ=3.4 at $Sr_c = 1.80$ as opposed to $C_l = 0.89$ for λ=3273 at the same Strouhal number. Flexibility also increases drag coefficient, although the level is relatively small, and increases power coefficient at low Strouhal numbers but decreases power coefficient at high Strouhal numbers with a crossover that depends on the degree of flexibility. For conciseness the deformation and velocimetry measurements will consider the two extreme low AR cases: λ=3273, termed 'rigid', and λ=3.4, termed 'flexible'. This flexible case was also chosen due to the very high lift coefficients at high Strouhal numbers.

3.2 Deformation measurements

Shown in Fig. 6 are the midchord positions for the low AR flexible wing for four representative Strouhal numbers, at twelve consecutive times. Solid lines represent

when the root is moving downwards; dashed lines represent data when the root is moving upwards. At $Sr_c = 0.600$ there is a downward bias along the span of the wing due to the deformation caused by the freestream velocity. At this low frequency there is a small amount of relative deformation due to the plunging motion. During the downward motion the wing bends upwards and during the upward motion it bends downwards, indicating that the tip lags the root. With the frequency increased to $Sr_c = 1.125$ (Fig. 6b) the total force is greater and there is therefore a greater difference between the up and down instants. Due to this greater deformation the amplitude of the tip motion is larger than the root amplitude. Increasing the Strouhal number to $Sr_c = 1.500$ (Fig. 6c) decreases the tip amplitude despite the deformation being greater. This is due to the increasing phase lag of the deformation, so even though the deformation is greater it is counteracted by the plunging motion of the wing. Increasing the Strouhal number to the maximum studied: $Sr_c = 2.025$ (Fig. 6d), the deformation increases again but the tip amplitude is decreased.

Shown in Fig. 7 are measurements of the variation of amplitude and phase lag along the span of the low AR flexible wing for all of the 27 Strouhal numbers tested. At low Strouhal numbers amplitude shows a parabolic trend with steeper gradient for larger Strouhal number. The tip amplitude therefore increases with increasing Strouhal number. After $Sr_c = 0.900$ however the initial gradient (at $z/s = 0$) begins to reduce with increasing Strouhal number. Despite this decrease in initial gradient, the gradient becomes steeper again further along the span. Thus, the tip amplitude continues to increase in this regime. At $Sr_c = 1.125$ the decrease in initial gradient results in a negative initial gradient. There is therefore an inflexion point at $z/s \approx 0.2$. This Strouhal number corresponds to the peak tip amplitude. Further increase beyond this Strouhal number is represented by a dashed line and results in a greater negative initial gradient, a smaller minimum, and reducing tip amplitude. Phase lag consistently increases along the span with an inflexion point at $z/s \approx 0.5$. The phase lag also consistently increases with Strouhal number. Measurements are not shown for the rigid wing as the amplitude ratio is $a_z/a_{root} = 1$ and the phase lag is $\theta = 0°$ across the span by definition.

Shown in Fig. 8 is the tip amplitude ratio (solid line) and tip phase lag (dashed line) against Strouhal number for both low and high AR flexible wings. For the low AR wing initially the amplitude ratio consistently increases reaching a maximum at $Sr_c = 1.125$ of $a_{tip}/a_{root} = 1.70$, and then decaying after. The tip phase lag consistently increases. For

this wing the natural frequency was measured as $Sr_c \approx 1.54$. This is larger than the frequency corresponding to peak tip amplitude; however one would expect this behaviour in a system with damping. The tip phase-lag of 90° at $Sr_c \approx 1.43$ does however lie within the uncertainty range for the natural frequency. For the high AR wing the same trends are observed except the peak amplitude ratio is slightly higher and later at $a_{tip}/a_{root} = 1.93$ and $Sr_c = 1.350$ and the tip phase lag is slightly lower. More detailed measurements for this wing can be found in Cleaver *et al.* (2013b) but it is qualitatively similar to the low AR wing. For the high AR wing the natural frequency was measured as $Sr_c \approx 1.5$. The Strouhal number $Sr_c = 1.500$ was therefore selected for flow field measurements due to the high lift experienced (see Fig. 5) and it being close to the measured natural frequency of both flexible wings. At this Strouhal number the low AR wing experiences a tip phase lag of $\theta_{tip} = 98°$ and amplitude of $a_{tip}/a_{root} = 1.53$; and the high AR wing experiences a tip phase lag of $\theta_{tip} = 91°$ and amplitude of $a_{tip}/a_{root} = 1.84$.

3.3 Velocity measurements

Shown in Fig. 9 are isosurfaces of phase-averaged vorticity magnitude for the low AR rigid wing (left) and flexible wing (right) for twelve phases in the cycle. These isosurfaces are colored by contours of spanwise vorticity. Blue therefore represents clockwise rotation (looking from the tip towards the root), and red counter-clockwise rotation. The phases start with the top of the motion ($t/T = 0/12$) moving down to the bottom of the motion ($t/T = 6/12$) before moving back up to reset the motion at the top. The column on the left shows the effective angle of attack across the span of the wing. This includes the root angle of attack, geometric twist and local plunge velocity. For the rigid wing, the root and tip move in-phase and the effective angle of attack is therefore constant across the span (dashed line). For the flexible wing, the root and tip move out-of-phase and it therefore varies across the span (solid line).

Starting with the rigid wing at the top of the motion ($t/T = 0/12$), in the wake are the remnants of the trailing-edge and tip vortices from the previous cycle. Likewise there is a region of clockwise vorticity near the leading-edge which is the remnants of a previous LEV, and below the tip are remnants of the previous tip vortex. This tip vortex is coloured green because there is minimal rotation around the z-axis. As the wing begins to move downwards ($t/T = 1/12$ to $3/12$) these remnants convect downstream

and either leave the measurement volume or lose their coherency. In addition a new TEV and tip vortex form and grow in strength. More interestingly a very strong LEV forms very rapidly and appears to detach from the wing by t/T = 3/12 despite the wing continuing to move downwards until t/T = 6/12. For t/T = 2/12 to 6/12 a vortex ring is observed at the leading edge in the region z/c < 0.7. This vortex ring is more clearly demonstrated from an upstream perspective in Fig. 10. This ring links the primary clockwise LEV with the counter-clockwise upper-surface LEV from the previous cycle. This vortex loop encircles the primary LEV drawing it upstream and away from the airfoil surface. Considering only the near root flow this behaviour is very similar to the LEV dipole previously observed for an infinite flat plate airfoil (Cleaver *et al*., 2013a). This LEV dipole is responsible for the large decrease in lift for $Sr_c \geq 0.975$ shown by the infinite wing case in Fig. 5a. It is caused by the upper surface clockwise vortex forming a dipole with the counter-clockwise lower surface LEV. This dipole convects in an upstream direction resulting in the rapid dissipation of both vortices to leave a 'plume' of vorticity. As discussed in the introduction, similar behaviour has also been observed for finite wings (Calderon *et al*., 2013a). In this case, the experimental conditions were slightly different: α = 20° instead of 15°, Re = 20,000 instead of 10,000, and Sr_c = 1.350 instead of 1.500. Nevertheless a LEV ring is still present for sAR = 2. However, for finite wings the behavior is complicated by the three-dimensionality introduced by the tip which necessitates the dipole to close on itself thereby forming a vortex ring. Nevertheless the result is the same, an upper surface LEV that pairs with the lower surface LEV to form a ring that convects upstream and away from the upper surface resulting in low lift.

Shown in the right column are isosurfaces for the flexible wing. Note the higher values of isosurface levels of vorticity. In this case the tip lags the root by 98°. The root reaches the extremes of its motion at t/T = 0/12 and 6/12; whereas the tip reaches the extremes of its motion at $t/T \approx$ 3/12 and 9/12. At the top of the root motion (t/T = 0/12) there is still a strong LEV from the previous cycle close to the upper surface. Comparing with the equivalent rigid wing the difference in LEV behaviour is very apparent. For the flexible wing there is a strong coherent LEV which convects close to the upper surface. As shown clearly in t/T = 1/12 and 2/12 this LEV is connected to the tip vortex from the lower surface, note that the tip is still moving upwards during these phases. As the root moves downwards (between t/T = 1/12 and 3/12) the LEV convects

downstream and a counter-clockwise TEV and clockwise LEV begin to form near the root. The LEV and TEV are only partially captured in the volumetric measurements due to their proximity to the wing surface. Once the tip reaches the top of its motion (t/T = 3/12), the LEV disconnects from the tip vortex and instead closes on the upper surface. Conversely the lower surface tip vortex disconnects from the LEV and instead connects to the upper surface tip vortex that is beginning to form due to the downward motion of the tip. This is more clearly visible at t/T = 4/12. During this downward motion the LEV and TEV spread from the root towards the tip (t/T = 4/12 to 6/12). Once the root reaches the bottom of its motion, the LEV and TEV are shed from the root but continue to grow further outboard, this is most clearly visible at time: t/T = 9/12. In addition the previous lower surface tip vortex continues to wrap itself around the upper surface tip vortex to form a vortex loop (see t/T = 8/12). Once the tip reaches the bottom of its motion (t/T = 9/12), the LEV and TEV are shed completely. By direct comparison of the rigid and flexible wings it is clear that the flexible wing does not experience a LEV ring. Instead a strong LEV forms and convects close to the upper surface which is commensurate with the higher lift. Throughout this entire process the formation and shedding of both LEV and TEV is closely aligned with the local effective angle of attack. Hence, both LEV and TEV initially form at the root and then grow outwards as the effective angle of attack increases along the span.

LEV stabilization and attachment for flapping wings is thought to be driven by the transport of LEV vorticity to the wing tip via the spanwise velocity component of the LEV, see Carr et al. (2013). This spanwise velocity is on the order of the wing tip velocity and driven by a spanwise pressure gradient. To investigate if spanwise velocity causes the stabilization of the LEV for the flexible case, shown in Fig. 11 are the same isosurfaces of phase-averaged vorticity magnitude but overlaid with spanwise velocity normalized by the freestream velocity. Positive represents velocity from the root towards the tip. For the rigid wing the only significant spanwise velocity is that due to the tip vortex roll-up. Slices through the LEV, not shown here, show minimal spanwise velocity within the LEV across all phases. The flexible wing LEV is first visible near the root at t/T = 3/12 and initially has small levels of spanwise velocity near the tip due to the tip vortex roll-up (see t/T = 5/12 to 12/12). After it has shed the level of spanwise velocity increases as shown by the LEV from the previous cycle during the time t/T = 5/12 to 9/12. As previously noted the primary difference between the rigid and flexible

cases is the presence / absence of the vortex ring. For the rigid wing the vortex ring forms and sheds very quickly, during t/T = 0/12 to 4/12. Although it cannot be excluded as a possibility, the low level of spanwise velocity in the core of the forming LEV combined with the lag between the occurrence of spanwise flow and LEV formation would indicate that spanwise velocity is not responsible for preventing vortex ring formation in the case of the flexible wing.

Shown in Fig. 12 are similar flow field measurements for the high aspect ratio rigid and flexible wings. For the rigid wing (left column), the root and tip move in-phase. Starting with the top of the motion (t/T = 0/12), behind the trailing-edge there is a region of clockwise vorticity. This is the remnants of a TEV formed during the upward motion which has now convected outside the measurement volume. Above the leading-edge there are weak regions of clockwise vorticity a large distance above the leading-edge. This appears to be the remnants of a clockwise upper-surface LEV. Once the wing begins moving downwards (t/T = 0/12 to 3/12) a new LEV begins to form and move upstream due to the other LEV from the lower surface. This LEV is accompanied by a tip vortex and TEV. The phase t/T = 3/12 is the point of maximum downwards velocity, as such there is a strong counter-clockwise TEV and tip vortex. Similar to the lower AR case the LEV is part of a vortex ring but this is only partially captured because it is upstream of the leading edge and due to the viewing angle. With further progression downwards (t/T = 3/12 to 6/12) the LEV ring convects upwards away from the upper-surface losing its coherency and the tip vortex and TEV continue to grow becoming strongest at t/T = 6/12. The LEV is now fully captured inside the measurement volume. It is relatively weak and a large distance from the upper-surface. With the wing moving upwards (t/T = 6/12 to 0/12) the counter-clockwise TEV and tip vortex convect downstream and a new clockwise TEV forms (partially obscured by the convecting counter-clockwise TEV).

Now let us consider the high AR flexible wing (Fig. 12 right column). Due to the generally larger vorticity levels in this case it was necessary to raise the isosurface levels relative to the rigid wing. The deformation of the wing gives a phase lag of θ = 91° so that the tip lags behind the root wing by $t/T \approx 3/12$. Therefore, at t/T = 0/12 the root has reached the top of the motion and has zero vertical velocity, whereas the tip is passing through the centre of its motions and has maximum upward velocity. In this phase, there is a clear TEV, tip vortex, and a much stronger region of clockwise vorticity

over the upper surface indicative of an LEV. The strengths of all three are greater than those observed for the rigid wing. As the root moves downwards (t/T = 0/12 to 3/12) the tip moves upwards strengthening the tip vortex from the lower surface. The LEV convects downstream dissipating as it progresses. At t/T = 3/12 the root is moving downwards with maximum velocity whilst the tip has reached the top of its motion. The lower surface tip vortex can be observed below the tip, and an upper surface tip vortex is beginning to form near the tip. As the tip begins to move downwards (t/T = 3/12 to 6/12) this upper surface tip vortex grows in strength the new upper surface LEV grows in strength. As the root moves upwards (t/T = 6/12 to 9/12) the tip continues to move downwards reaching the bottom of its motion at t/T = 9/12. There is a strong counter-clockwise TEV formed during the downward motion which is shed first from the root and later from the tip. There is a very complex tip vortex similar to those described in Calderon *et al.* (2012), and a relatively strong clockwise LEV. For all three vortices the maximum levels of vorticity are significantly higher than those observed for the rigid wing, especially taking into account the higher isosurface levels. In a similar manner to the low AR wing, the significantly higher lift can therefore be attributed to the flexibility inhibiting LEV ring formation, resulting in a stronger upper surface LEV that convects closer to the upper surface, and a stronger tip vortex (Shyy *et al.*, 2009).

4. Conclusions

For wings periodically plunging with small-amplitude at the root, spanwise flexibility can substantially increase time-averaged lift in the post-stall regime. The increase in lift coefficient over the stationary case is strongly dependent on Strouhal number. For low (AR = 3) aspect ratio the peak lift coefficient was C_l = 2.77 for the λ = 3.4 flexible wing at $\mathrm{Sr_c}$ = 1.8 as opposed to C_l = 0.89 for the rigid wing at the same Strouhal number, a more than three-fold improvement through flexibility. For high (AR = 6) aspect ratio the largest recorded was C_l = 3.14 for the flexible wing as opposed to C_l = 1.04 for the rigid wing at the same Strouhal number. This improvement is associated with significant deformation of the wing. Generally this deformation causes the root amplitude to be amplified along the span leading to a larger amplitude tip motion but with a phase lag. For both aspect ratios, a Strouhal number of Sr_c = 1.5 was

selected for detailed volumetric velocimetry measurements because it shows a comparatively large increase in lift coefficient for the flexible wing and is close to the flexible wing's natural frequency. For this Strouhal number both low and high AR rigid wings exhibit a complex three-dimensional LEV dipole / ring. This is where the upper surface clockwise LEV forms a vortex ring with the lower surface counter-clockwise LEV. This vortex ring self-advects upstream and away from the upper surface explaining the low lift coefficient. Conversely the flexible wings exhibit a strong LEV that convects close to the upper surface. It can therefore be concluded that, in this case, flexibility acts to inhibit the LEV ring and thus create a high lift scenario.

Acknowledgements

The authors would like to acknowledge support from the Air Force Office of Scientific Research, Air Force Material Command, USAF under grant number FA8655-09-1-3007, and the EPSRC loan pool.

References

Baek, S.J., Lee, S.J., 1996. A New Two-Frame Particle Tracking Algorithm Using Match Probability. Exp. Fluids 22, No. 1, 23-32.

Barnes, C.J., Visbal, M., Gordnier, R.E., 2013. High-Fidelity Simulations of a Flexible, Heaving Finite-Aspect-Ratio Wing. AIAA-2013-3179, 43rd AIAA Fluid Dynamics Conference, San Diego, CA.

Biewener, A.A., Dial, K.P., 1995. In-Vivo Strain in the Humerus of Pigeons (Columba-Livia) During Flight. J. of Morphology 225, No. 1, 61-75.

Calderon, D.E., Wang, Z., Gursul, I., 2012. Volumetric Measurements and Simulations of the Vortex Structures Generated by Low Aspect Ratio Plunging Wings. AIAA-2012-914, 50th AIAA Aerospace Sciences Meeting.

Calderon, D.E., Wang, Z., Gursul, I., 2013a. Lift-Enhancing Vortex Flows Generated by Plunging Rectangular Wings with Small Amplitude. AIAA J. 51, 2953-2964.

Calderon, D.E., Wang, Z., Gursul, I., Visbal, M.R., 2013b. Volumetric measurements and simulations of the vortex structures generated by low aspect ratio plunging wings. Phys Fluids 25.

Carr, Z.R., Chen, C., Ringuette, M.J., 2013. Finite-span rotating wings: three-dimensional vortex formation and variations with aspect ratio. Exp. Fluids 54, 1-26.

Chimakurthi, S.K., Tang, J., Palacios, R., Cesnik, C.E.S., Shyy, W., 2009. Computational Aeroelasticity Framework for Analyzing Flapping Wing Micro Air Vehicles. AIAA J. 47, No. 8, 1865-1878.

Cleaver, D.J., Wang, Z., Gursul, I., 2011. Lift Enhancement by Means of Small Amplitude Airfoil Oscillations at Low Reynolds Numbers. AIAA J. 49, No. 9, 2018 - 2033.

Cleaver, D.J., Wang, Z., Gursul, I., 2013a. Investigation of High-Lift Mechanisms for a Flat-Plate Airfoil Undergoing Small-Amplitude Plunging Oscillations. AIAA J. 51, 968-980.

Cleaver, D.J., Wang, Z., Gursul, I., 2013b. Oscillating Flexible Wings at Low Reynolds Numbers, 51st AIAA Aerospace Sciences Meeting, Grapevine, Texas.

Cleaver, D.J., Gursul, I., Calderon, D.E., Wang, Z., 2014. Thrust enhancement due to flexible trailing-edge of plunging foils. Journal of Fluids and Structures 51, 401-412.

Frampton, K.D., Goldfarb, M., Monopoli, D., Cveticanin, D., 2002. Passive aeroelastic tailoring for optimal flapping wings, in: Fixed and Flapping Wing Aerodynamics for Micro Air Vehicle Applications. Amer Inst Aeronautics & Astronautics, Reston.

Gordnier, R.E., 2009. High Fidelity Computational Simulation of a Membrane Wing Airfoil. J. of Fluids and Structures 25, No. 5, 897-917.

Gursul, I., Cleaver, D.J., Wang, Z., 2014. Control of low Reynolds number flows by means of fluid-structure interactions. Prog. Aerosp. Sci. 64, 17-55.

Heathcote, S., 2006. Flexible Flapping Airfoil Propulsion at Low Reynolds Numbers, Ph.D. Thesis, Dept of Mechanical Engineering, University of Bath, Bath, UK.

Heathcote, S., Gursul, I., 2007. Flexible Flapping Airfoil Propulsion at Low Reynolds Numbers. AIAA Journal 45, No. 5, 1066-1079.

Heathcote, S., Wang, Z., Gursul, I., 2008. Effect of Spanwise Flexibility on Flapping Wing Propulsion. J. of Fluids and Structures 24, No. 2, 183-199.

Ho, S., Nassef, H., Pornsinsirirak, N., Tai, Y.C., Ho, C.M., 2003. Unsteady Aerodynamics and Flow Control for Flapping Wing Flyers. Progress in Aerospace Sciences 39, No. 8, 635-681.

Moffat, R.J., 1988. Describing the Uncertainties in Experimental Results. Exp. Thermal and Fluid Sci. 1, No. 1, 3-17.

Mountcastle, A.M., Daniel, T.L., 2009. Aerodynamic and Functional Consequences of Wing Compliance. Exp. in Fluids 46, No. 5, pp. 873-882.

Pereira, F., Gharib, M., 2002. Defocusing Digital Particle Image Velocimetry and the Three-Dimensional Characterization of Two-Phase Flows. Meas. Sci. & Tech. 13, No. 5, 683-694.

Pereira, F., Stuer, H., Graff, E.C., Gharib, M., 2006. Two-Frame 3d Particle Tracking. Meas. Sci. & Tech. 17, No. 7, 1680-1692.

Rojratsirikul, P., Genc, M.S., Wang, Z., Gursul, I., 2011. Flow-Induced Vibrations of Low Aspect Ratio Rectangular Membrane Wings. J. of Fluids and Structures 27, No. 8, 1296-1309.

Sane, S.P., 2003. The Aerodynamics of Insect Flight. J. of Exp. Biology 206, No. 23, 4191-4208.

Shyy, W., Berg, M., Ljungqvist, D., 1999. Flapping and Flexible Wings for Biological and Micro Air Vehicles. Progress in Aerospace Sciences 35, No. 5, 455-505.

Shyy, W., Trizila, P., Kang, C.K., Aono, H., 2009. Can Tip Vortices Enhance Lift of a Flapping Wing? AIAA J. 47, No. 2, 289-293.

Shyy, W., Aono, H., Chimakurthi, S.K., Trizila, P., Kang, C.K., Cesnik, C.E.S., et al., 2010. Recent Progress in Flapping Wing Aerodynamics and Aeroelasticity. Progress in Aerospace Sciences 46, No. 7, pp. 284-327.

Taylor, G., Wang, Z., Vardaki, E., Gursul, I., 2007. Lift Enhancement over Flexible Nonslender Delta Wings. AIAA J. 45, No. 12, 2979-2993.

Young, J., Lai, J.C.S., 2007. Mechanisms Influencing the Efficiency of Oscillating Airfoil Propulsion. AIAA J. 45, No. 7, 1695-1702.

Figures

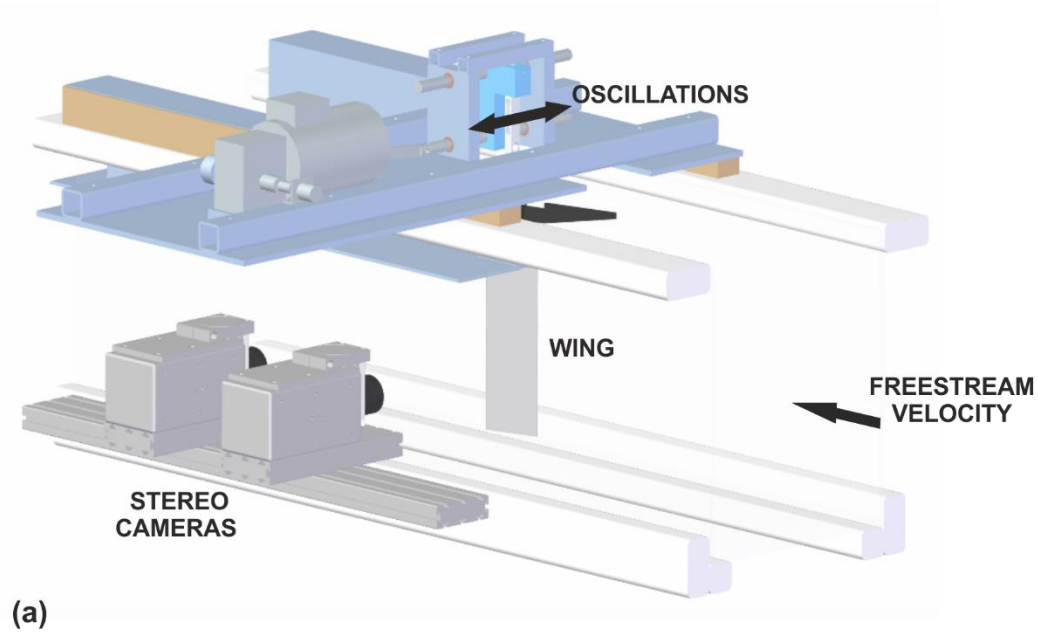

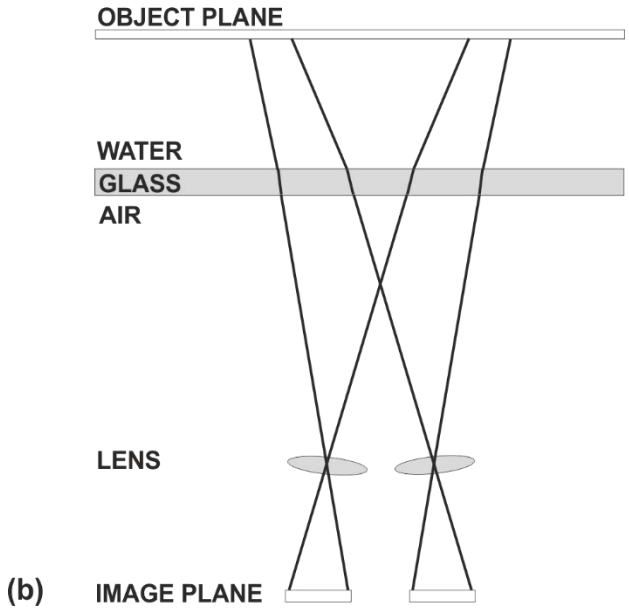

Fig. 1 (a) Digital image correlation setup, (b) method used to correct for image warping using Scheimpflug mounts. The maximum error was always less than 0.15%c.

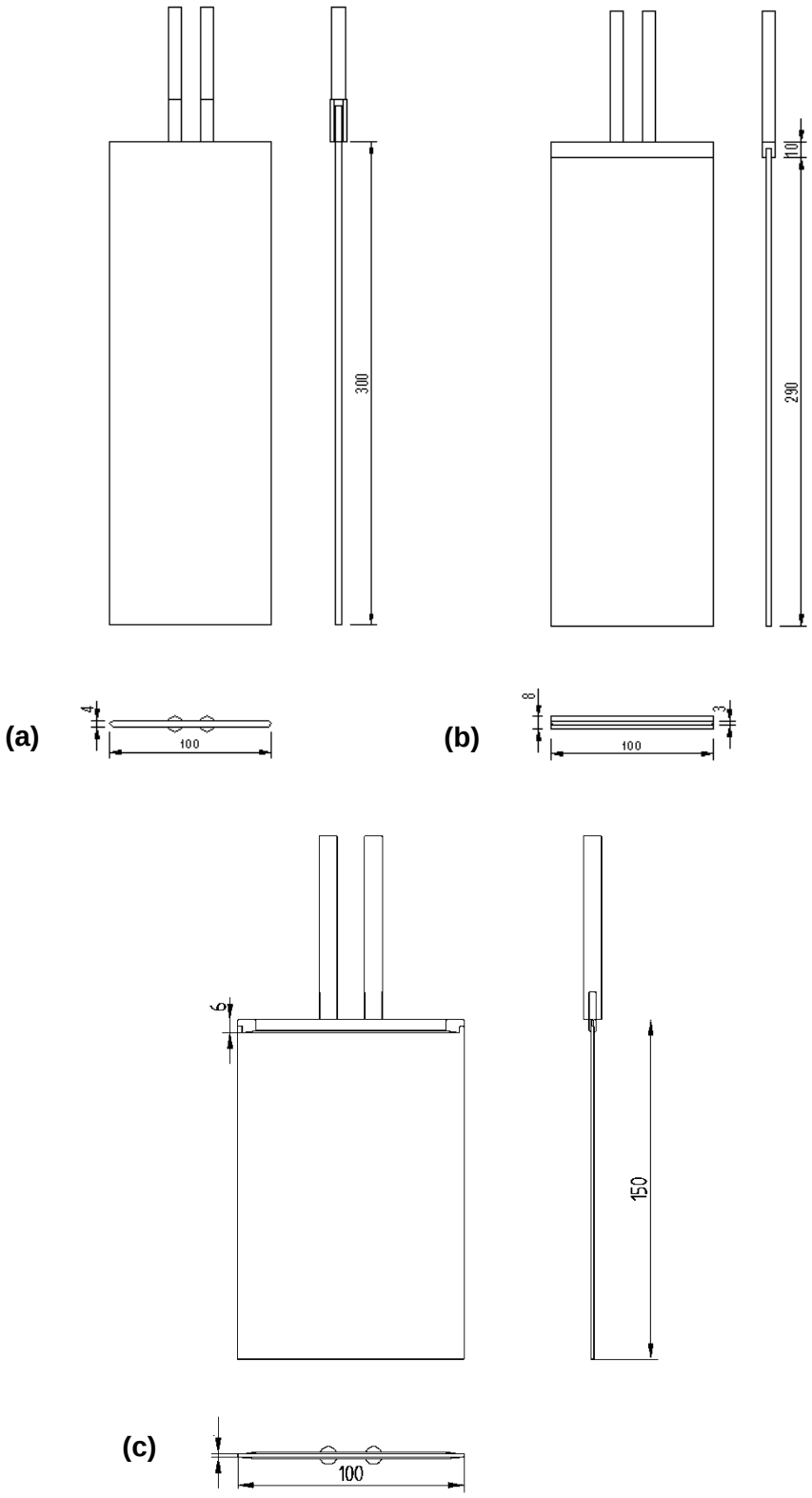

Fig. 2 Wing geometry: (a) *sAR* = 3 rigid wing, (b) *sAR* = 3 flexible wings and (c) *sAR* = 1.5 rigid (t=1.5mm) and flexible (t=1mm) wings.

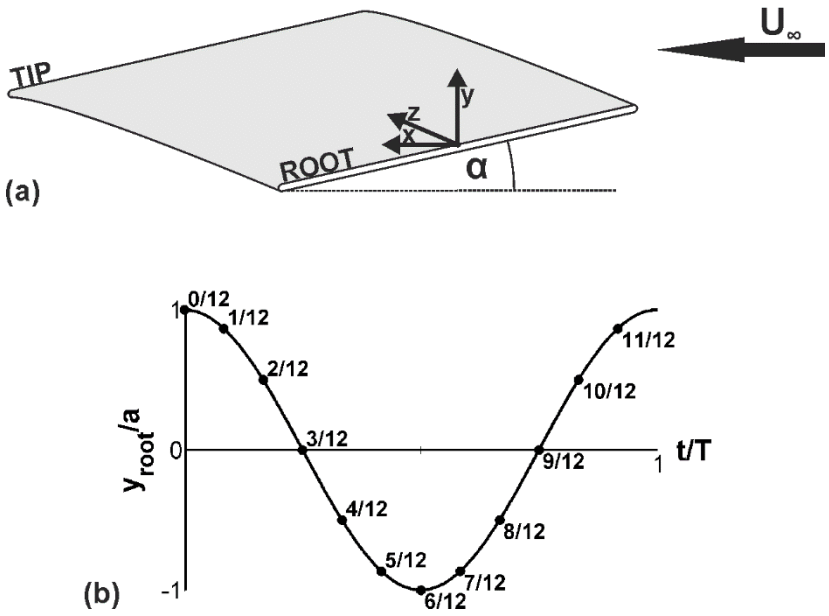

Fig. 3 Definition of parameters (a) the flexible wing was clamped rigidly along the root and oscillated sinusoidally with a fixed root angle of attack of *α* and amplitude of *a*; (b) definition of phases.

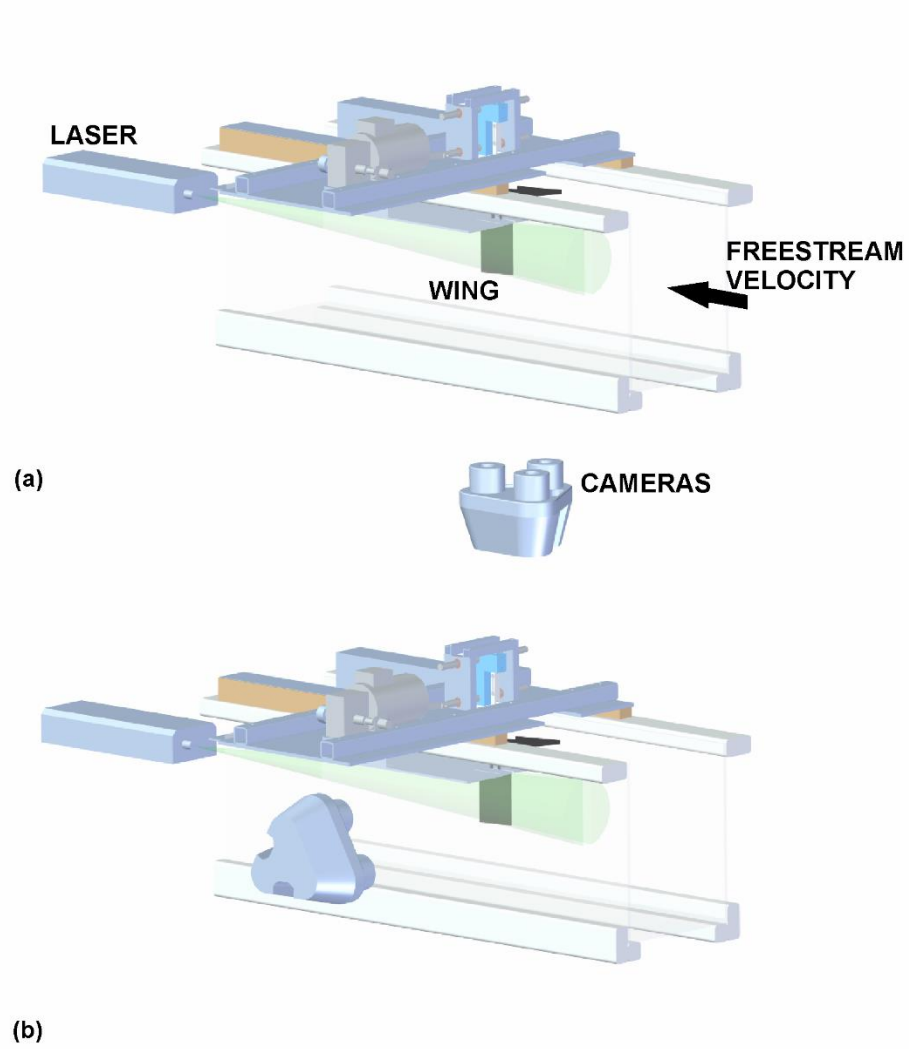

Fig. 4 Volumetric velocimetry setup.

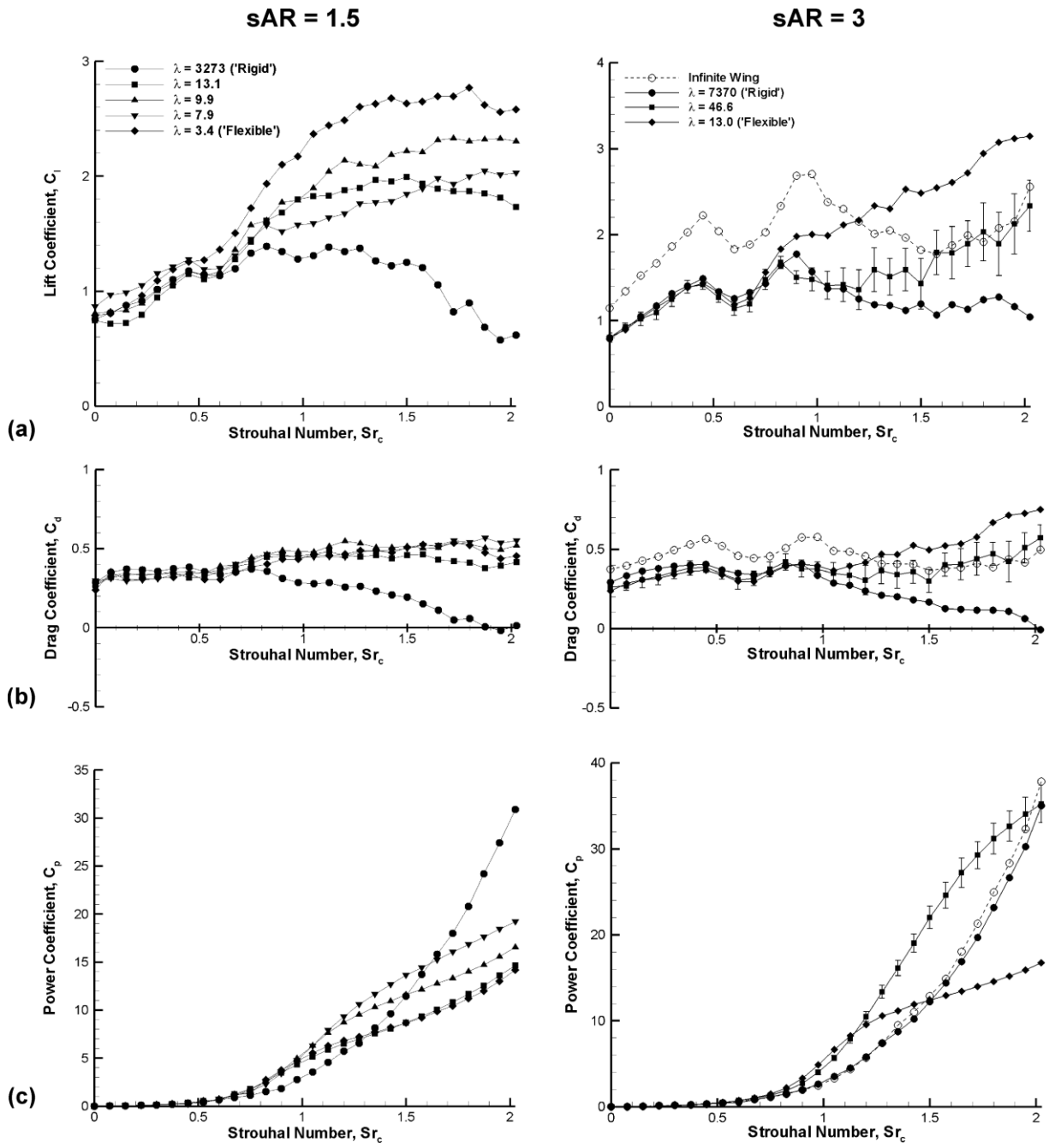

Fig. 5 Time-averaged (a) lift coefficient, (b) drag coefficient, and (c) power coefficient for the *sAR* = 1.5 (left column) and *sAR* = 3 (right column) wings.

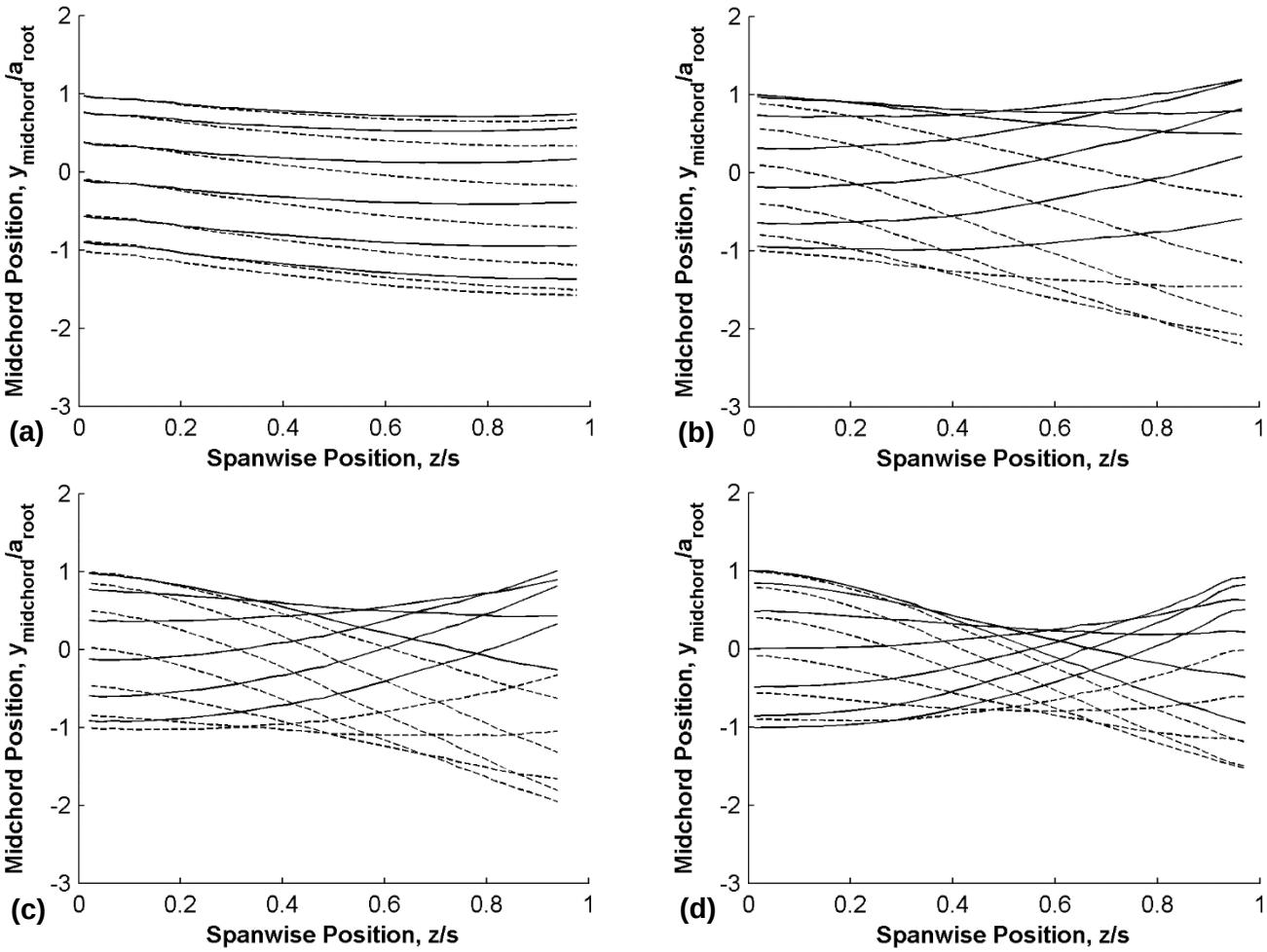

Fig. 6 Midchord position of the *sAR* = 1.5 flexible wing normalized by the root amplitude for twelve selected instants oscillating with: (a) Sr_c = 0.600, (b) Sr_c = 1.125, (c) Sr_c = 1.500 and (d) Sr_c = 2.025. Solid line is root moving downwards; dashed line is root moving upwards.

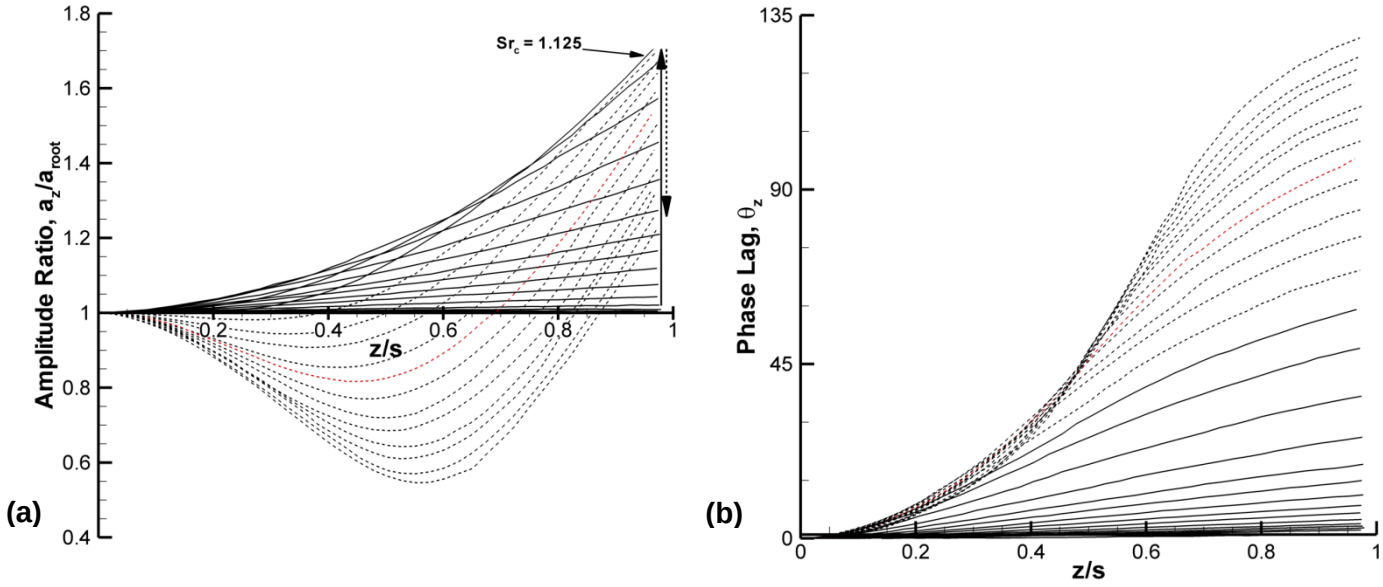

Fig. 7 (a) Amplitude ratio and (b) phase lag along the span of the *sAR* = 1.5 flexible wing for Strouhal numbers in the range Sr_c = 0.075 : 0.075 : 2.025. Solid lines are Strouhal numbers below the peak tip amplitude ($Sr_c \leq 1.125$); dashed lines are Strouhal numbers above the peak tip amplitude ($Sr_c > 1.125$). The red dashed line is Sr_c = 1.500.

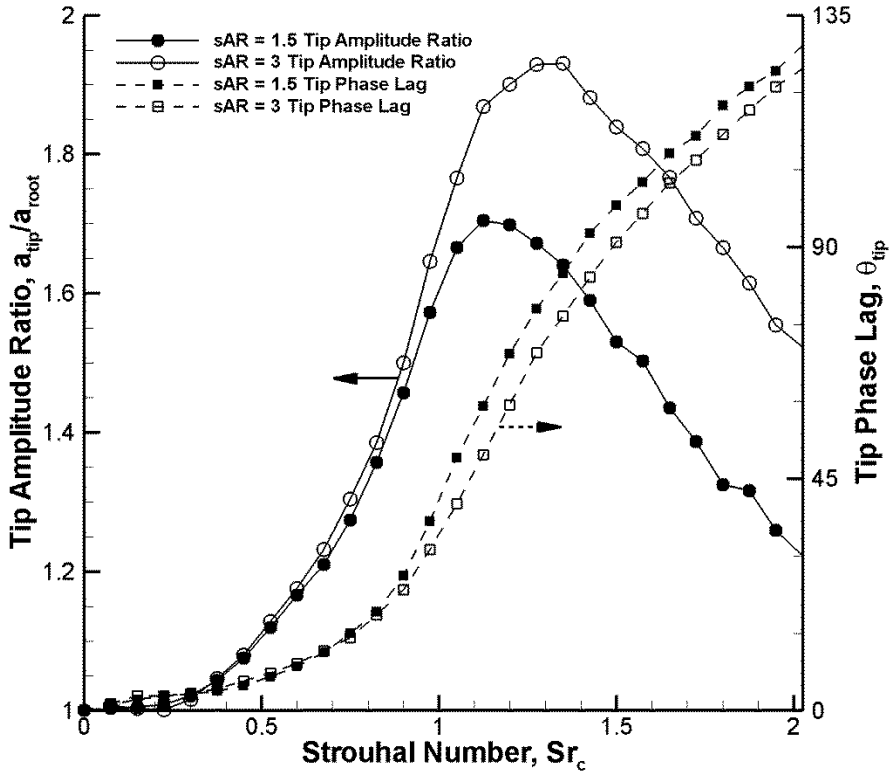

Fig. 8 Tip amplitude ratio (solid line) and tip phase lag in degrees (dashed line) against Strouhal number for the *sAR* = 1.5 and 3 flexible wings.

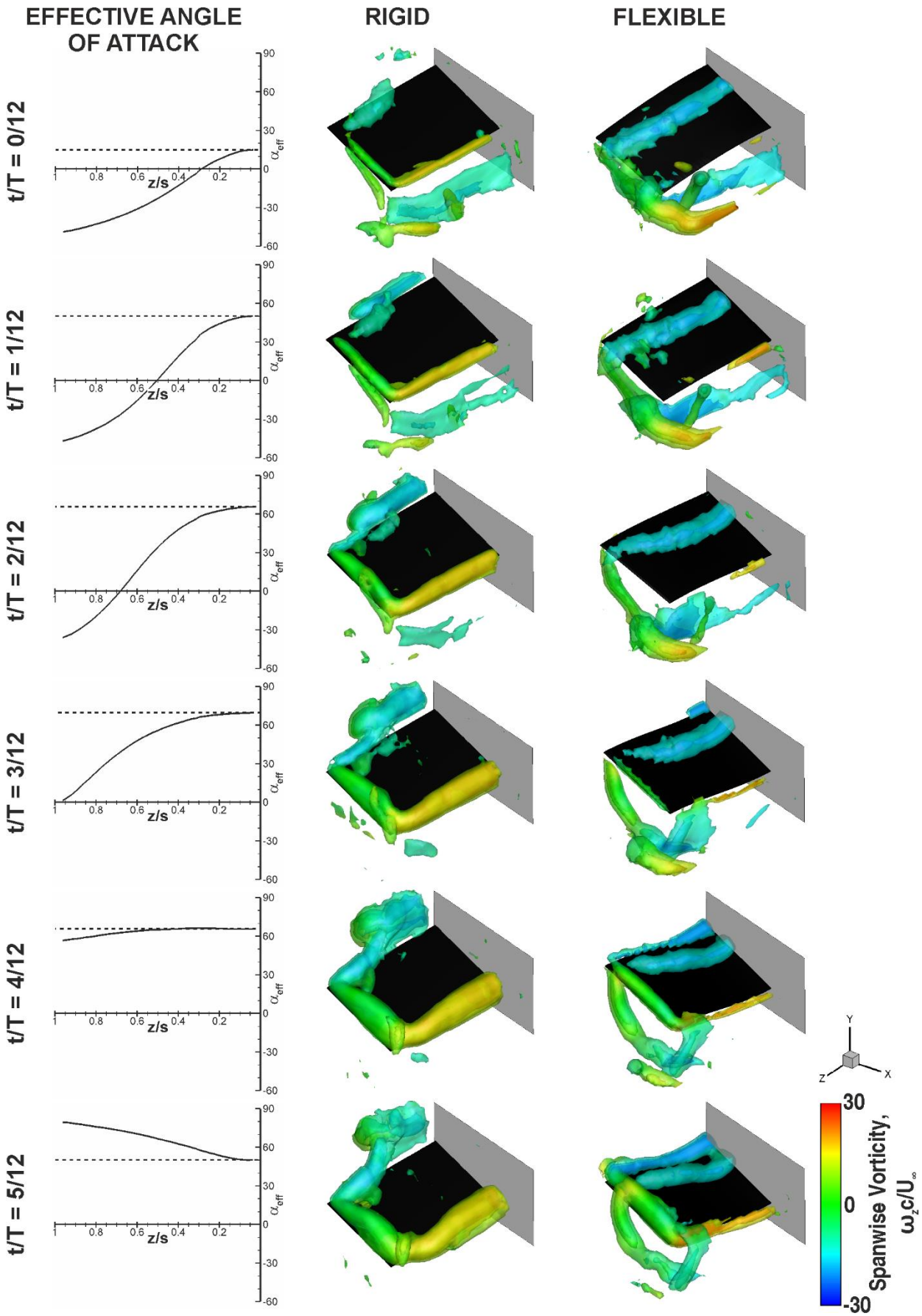

Fig. 9 Isosurfaces of phase-averaged vorticity magnitude (Rigid: $\omega c/U_\infty$ = 12, 20 and 28; Flexible: $\omega c/U_\infty$ = 15, 25 and 35) overlaid with spanwise vorticity for the *sAR* = 1.5 wings oscillating with Sr_c = 1.500.

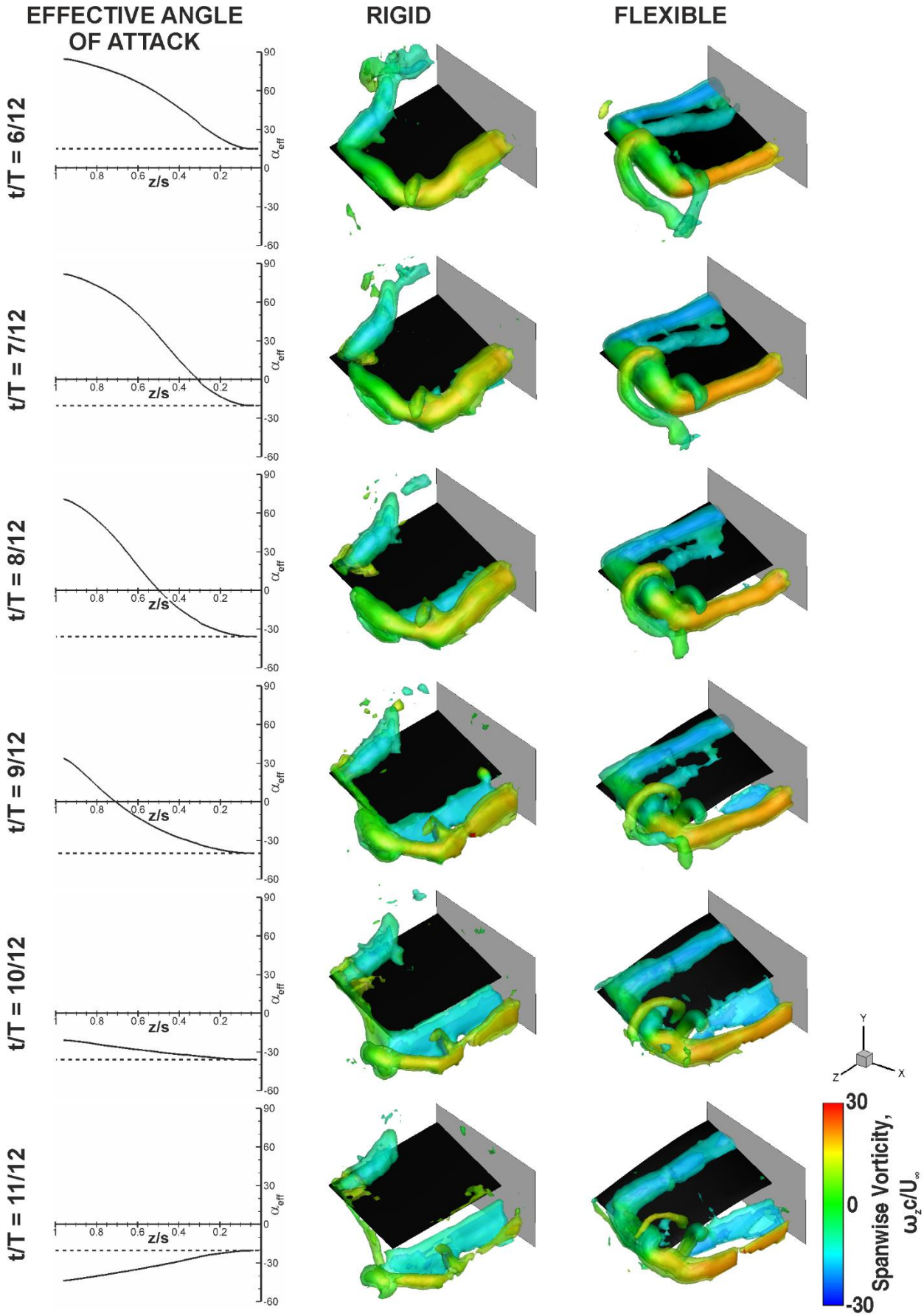

Fig. 9 Continued

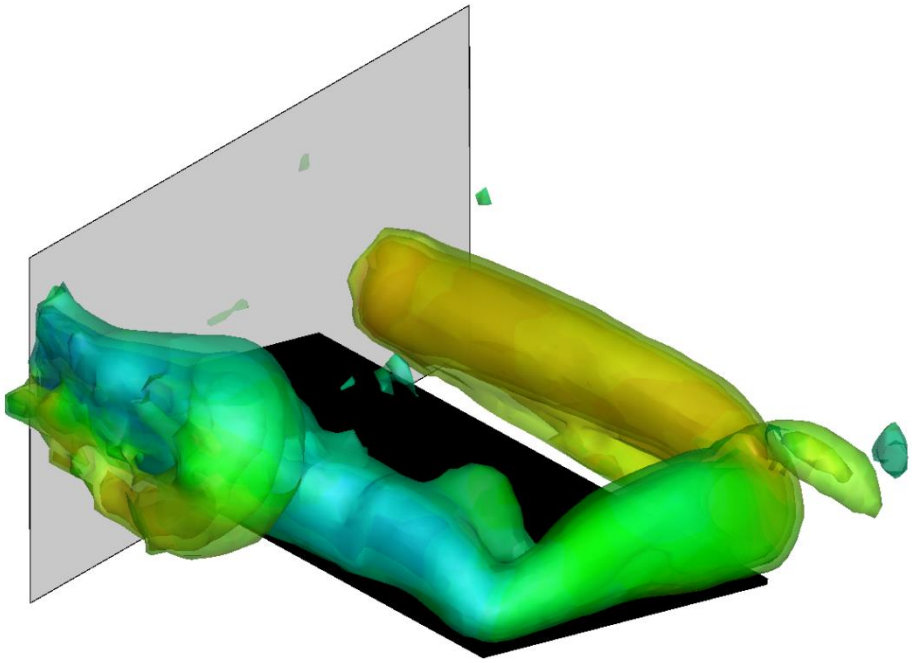

Fig. 10 LEV ring from an upstream perspective for *t/T* = 4/12. The lower surface counter-clockwise LEV has gone beyond the upstream edge of the volume and is therefore only partially captured.

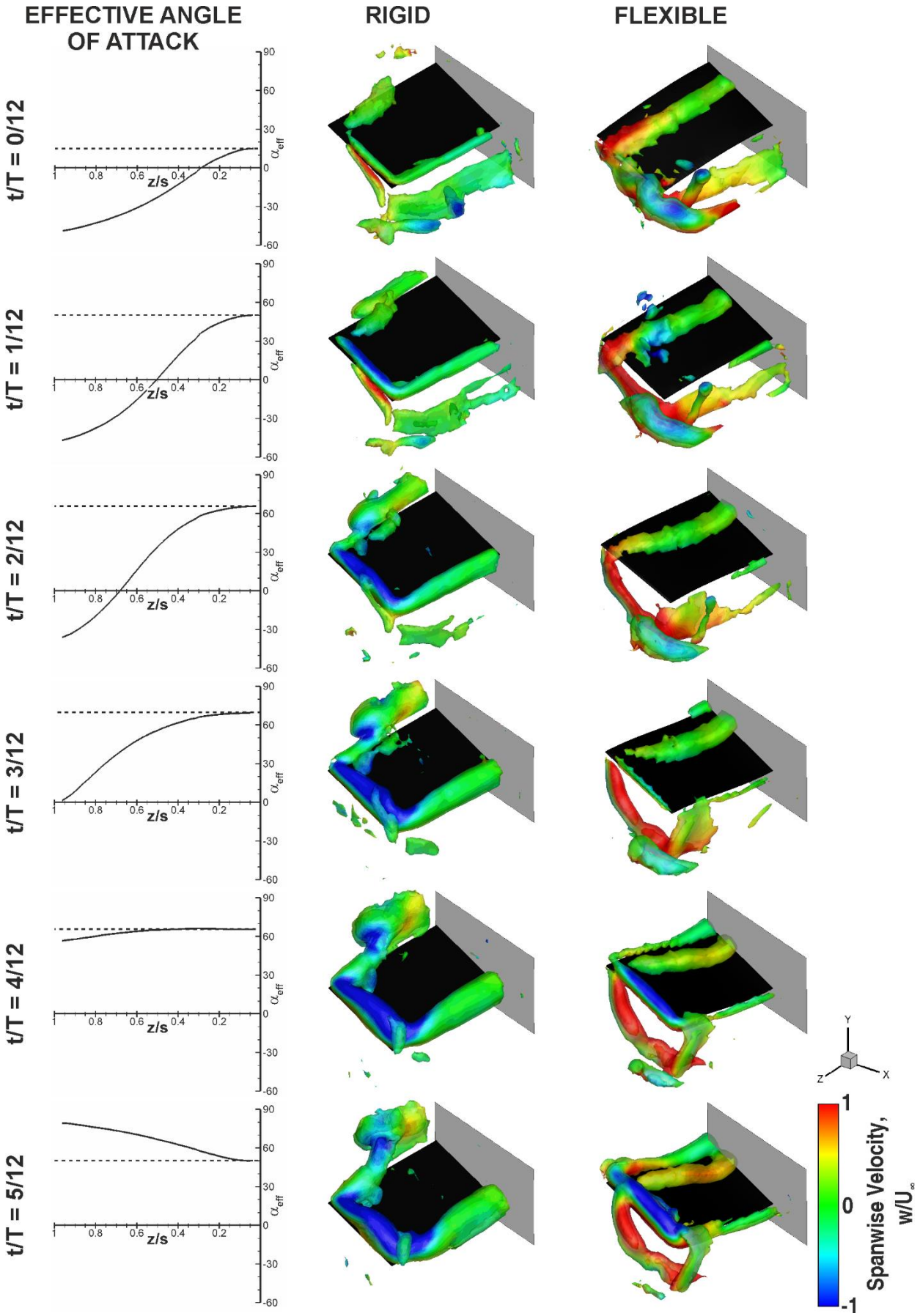

Fig. 11 Isosurfaces of phase-averaged vorticity magnitude (Rigid: $\omega c/U_\infty$ = 12, 20 and 28; Flexible: $\omega c/U_\infty$ = 15, 25 and 35) overlaid with spanwise velocity for the *sAR* = 1.5 wings oscillating with Sr_c = 1.500.

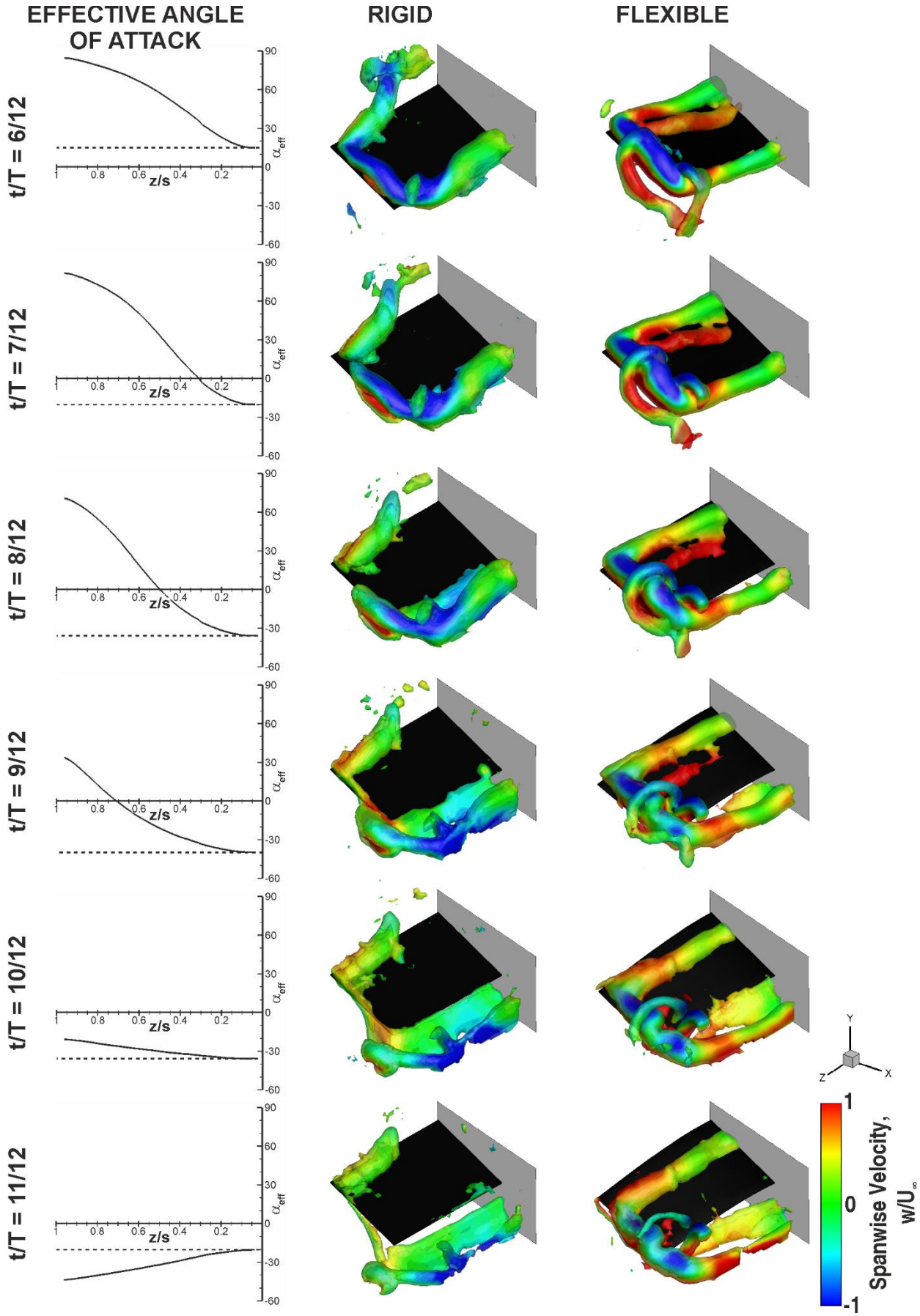

Fig. 11 Continued

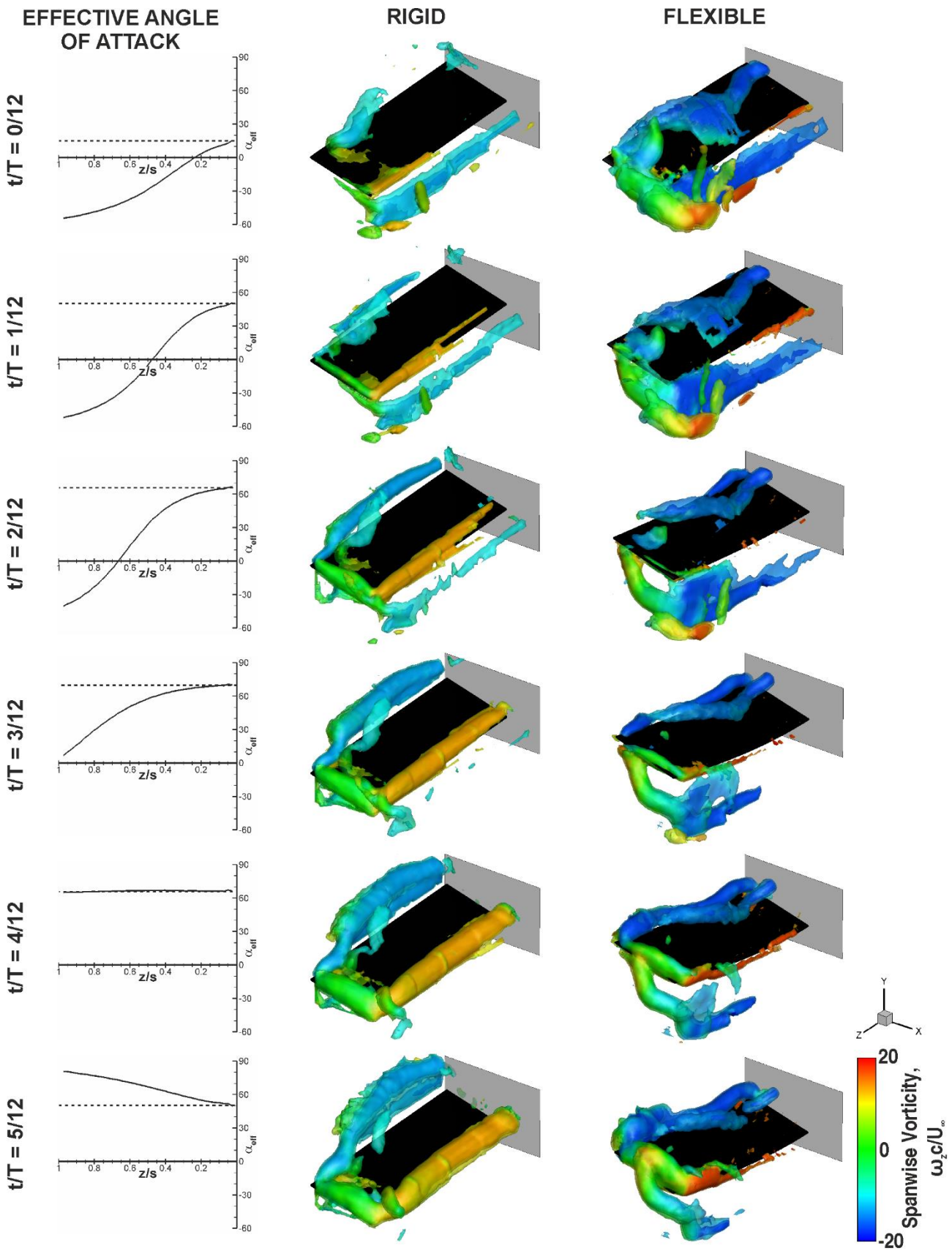

Fig. 12 Isosurfaces of phase-averaged vorticity magnitude (Rigid: $\omega c/U_\infty$ = 10, 15 and 20; Flexible: $\omega c/U_\infty$ = 15, 20 and 25) overlaid with spanwise vorticity for the sAR = 3 wings oscillating with Sr_c = 1.500.

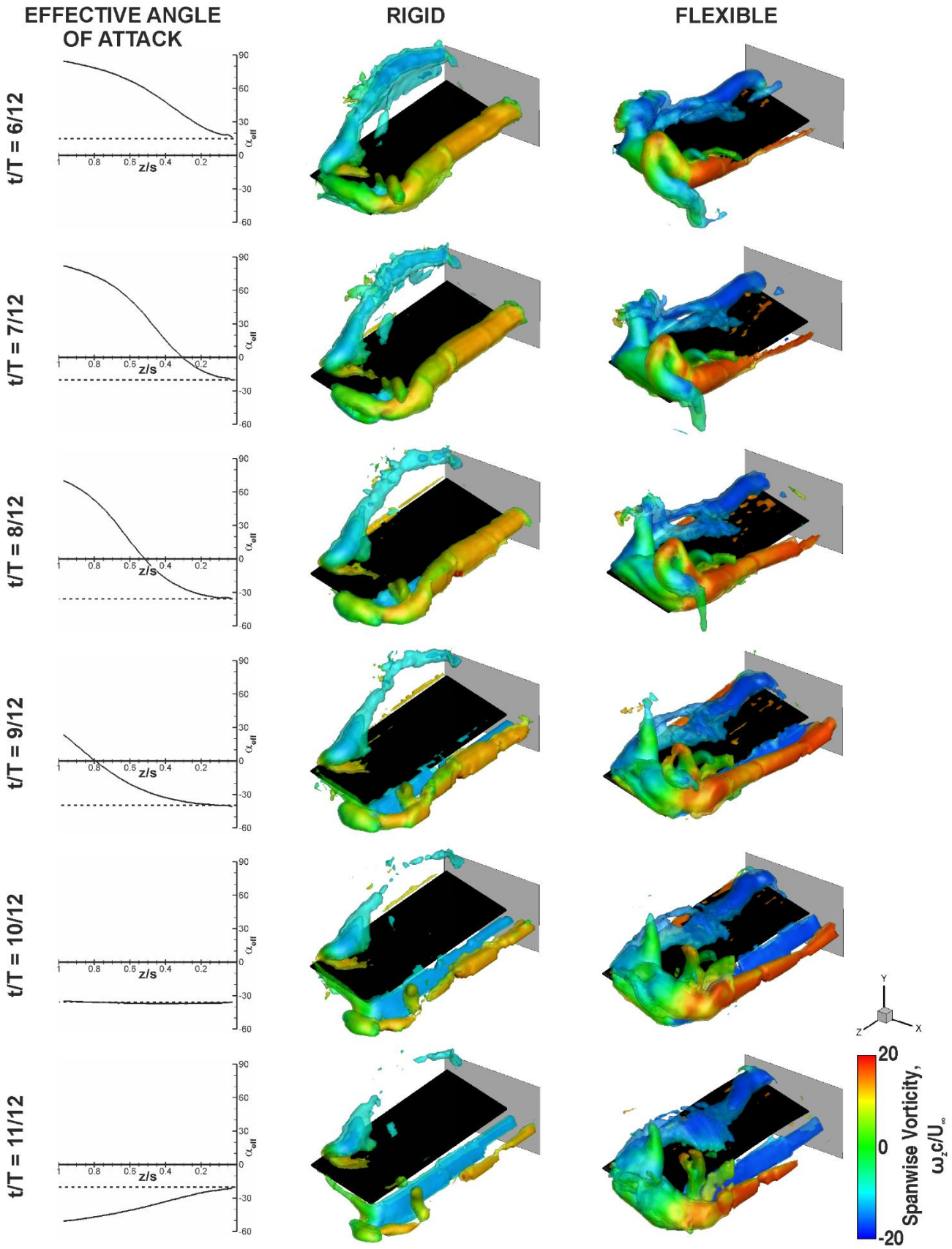

Fig. 12 Continued.